remote sensing

MDPI

Article

Climate-Specific Nonlinear Associations Between Urban Thermal Stress and the Built Environment Across Mainland China

Lige Qiao [1,2], Zhigao Zhou [3,4,*], Yao Chen [3,4] and Zhijiang Zhang [5]

[1] Faculty of Geographical Science and Engineering, College of Geographical Sciences, Henan University, Zhengzhou 450046, China; qiaolige@henu.edu.cn
[2] Key Laboratory of Geospatial Technology for the Middle and Lower Yellow River Regions, Ministry of Education, Henan University, Kaifeng 475004, China
[3] Collaborative Innovative Center for Emission Trading System Co-Constructed by the Province and Ministry, Hubei University of Economics, Wuhan 430205, China; chenyao@email.hbue.edu.cn
[4] Experimental Center for Resources and Environmental Technology, Hubei University of Economics, Wuhan 430205, China
[5] School of Geography Science and Geomatics Engineering, Suzhou University of Science and Technology, Suzhou 215009, China; zhangzhijiang@whu.edu.cn
* Correspondence: zhigao@hbue.edu.cn

Highlights

What are the main findings?

- Mean summer UTCI rose 0.82 °C from 2005 to 2020 across 1605 Chinese urban centres.
- NDVI ranked first in 2005 and 2010, and albedo in 2015 and 2020; built-environment associations varied across climate zones and years.

What are the implications of the main findings?

- Thermal-risk screening should be climate-specific, not based on uniform national thresholds.
- Identified response ranges need local validation before guiding urban design decisions.

Abstract

Urban thermal stress (UTS) is intensifying, but its evolution and relationships with the built environment may differ across China's contrasting climate zones. We examined mean summer Universal Thermal Climate Index (UTCI) estimates for 1605 urban centres identified in the Global Human Settlement Layer Urban Centre Database (GHS-UCDB) across mainland China in 2005, 2010, 2015, and 2020. Random Forest models and interpretable machine-learning methods were used to compare national patterns with those in two humid zones. Mean UTCI increased from 29.61 °C to 30.43 °C, and 73.02% of urban centres recorded higher values in 2020 than in 2005. The increase was concentrated in humid China, reaching 1.08 °C in the tropical–subtropical humid (TSH) zone and 0.64 °C in the temperate humid and semi-humid (TH) zone. Built-environment associations also differed across the four assessment years. Nationally, the normalized difference vegetation index (NDVI) ranked first in 2005 and 2010, whereas surface albedo ranked first in 2015 and 2020. Regional models showed sharper contrasts. NDVI and impervious-surface proportion consistently ranked highest in TSH, whereas albedo, urban morphology, and landscape configuration were more prominent in TH. Nonlinear responses and leading interactions varied across scales, zones, and years. National models showed predominantly NDVI-related patterns in 2005 and 2010, whereas albedo-related patterns were more prominent in 2015 and 2020. NDVI–impervious cover was the leading TSH interaction in 2010, 2015, and 2020. In TH, NDVI–population density ranked first in 2005 and 2010, tree cover–built-up intensity in 2015, and albedo–tree cover in 2020. National associations therefore cannot be transferred

Check for updates

Academic Editors: Shengjun Gao, Haiping Xia and Kangning Li

Received: 19 October 2026
Revised: 15 November 2026
Accepted: 18 November 2026
Published: 20 November 2026

Copyright: © 2026 by the authors. Licensee MDPI, Basel, Switzerland. This article is an open access article distributed under the terms and conditions of the Creative Commons Attribution (CC BY) license.

uniformly across climate zones. These findings support climate-specific thermal-risk screening, but model-derived response ranges require local validation before application in local urban planning and design decisions.

Keywords: urban thermal stress; Universal Thermal Climate Index; built environment; climate zones; nonlinear associations; interpretable machine learning

1. Introduction

Urban thermal stress (UTS) poses a growing threat to public health and urban livability amid ongoing climate warming and urbanization [1,2]. Global warming is increasing the frequency, intensity, and duration of extreme heat events [3,4]. Meanwhile, urban expansion replaces vegetation with impervious surfaces, increasing heat storage and altering surface-energy exchange [5,6]. As urban populations grow, these changes expose more people to hazardous thermal conditions and strain health systems, buildings, and infrastructure [7–9]. Understanding how UTS varies across space and time is therefore essential for climate-adaptive urban planning.

Large-scale urban heat assessments commonly rely on air temperature or land surface temperature [10–12]. Neither indicator fully captures human-perceived thermal conditions, which also depend on humidity, wind, and short-wave and long-wave radiation [13,14]. Thermal indices address this limitation by integrating multiple environmental variables. The Universal Thermal Climate Index (UTCI), for example, integrates meteorological conditions with models of human energy balance and thermophysiological responses [15–17]. It therefore represents outdoor thermal stress more comprehensively than temperature alone [18,19].

UTCI has been applied from individual cities to urban agglomerations, nations, and cross-national regions [2,18,20–24]. These studies have advanced our understanding of human thermal conditions, yet national-scale analyses face challenges in distinguishing the role of climatic background conditions from associations involving built-environment characteristics. UTCI responds to meteorological conditions that differ sharply among climate zones, while elevation and atmospheric circulation add further regional variation. Consequently, urban centres with similar built environments may experience different UTCI levels and temporal changes. However, systematic comparisons of UTCI patterns across China's major climate zones remain limited.

Climate may also modify how the built environment is associated with UTS. Landscape composition, spatial configuration, surface biophysical properties, urban morphology, and socioeconomic activity are associated with processes such as shading, evapotranspiration, heat storage, radiative exchange, and airflow [2,25,26]. However, many existing studies have focused on individual predictors or a limited range of built-environment characteristics. This narrow scope prevents direct comparison of their relative importance within a common framework. National models also combine urban centres with different climates and development patterns, whereas regional models describe relationships within narrower climatic ranges. Comparing both scales can distinguish broad national signals from climate-zone-specific associations.

Built-environment relationships with UTS are also rarely linear or independent. Associations involving vegetation, impervious cover, surface albedo, and urban morphology may exhibit nonlinear transitions or saturation effects and may vary with other urban characteristics [25,27]. Tree-based machine-learning models can capture these nonlinear relationships and higher-order interactions [28,29]. Model predictions can be further interpreted using SHapley Additive exPlanations (SHAP), marginal-response curves, and two-dimensional

partial dependence plots [30–32]. Few studies have compared these response patterns across multiple years and climate zones within a single analytical design.

These gaps raise a central question: How do the associations between the built environment and urban thermal stress differ across climatic contexts and assessment years? Addressing this question requires a consistent analytical framework that combines comparable urban units, repeated observations, multidimensional predictors, and climate-zone-specific modelling.

We addressed this question using GloUTCI-M summer estimates for 1605 urban centres identified in the Global Human Settlement Layer Urban Centre Database (GHS-UCDB) across mainland China in 2005, 2010, 2015, and 2020. We first characterized the spatiotemporal variation of UTCI across the national sample, population-size classes, and four climate zones. We then used Random Forest models and SHAP-based interpretation to compare predictor importance between the national model and the TSH and TH climate-zone models. Marginal-response curves and pairwise interaction analyses were further used to characterize differences in nonlinear associations and leading joint responses across models and assessment years. The findings provide evidence of climate-zone-specific heterogeneity in built-environment associations with urban thermal stress and may inform regional thermal-risk screening and further investigation of model-derived response ranges under local conditions.

2. Data and Methods

2.1. Study Area and Analytical Units

The analysis included 1605 urban centres in mainland China from GHS-UCDB. In this study, the term "urban centre" follows the official terminology of GHS-UCDB and refers to a spatially delineated, grid-based urban settlement unit rather than the downtown area, central business district, or administrative centre of a city. We calculated mean summer UTCI within fixed urban-centre boundaries for 2005, 2010, 2015, and 2020. According to China's national climate regionalization, 887 urban centres were located in the tropical–subtropical humid (TSH) zone, 624 in the temperate humid and semi-humid (TH) zone, 88 in the temperate arid and semi-arid (TA) zone, and 6 in the Tibetan Plateau (TP) region (Figure 1). All four zones contributed to the descriptive comparison. Regional machine-learning analyses focused on TSH and TH because the TA and TP samples were too small for comparably stable models.

Following earlier population-based classifications [33,34], we grouped the sampled urban centres into three population-size classes: medium cities (fewer than 1 million residents), large cities (1 million to fewer than 5 million residents), and supercities (5 million residents or more) (Figure 1). These labels refer only to the population of the analytical units and do not indicate administrative status.

Urban boundaries came from the 2024 edition of GHS-UCDB, developed by the European Commission's Joint Research Centre [35]. The analytical units were selected directly from GHS-UCDB rather than extracted from administrative city boundaries. We first identified urban centres located in mainland China and verified their presence in 2005, 2010, 2015, and 2020. As an independent quality-control check, we compared these polygons with impervious surfaces in the 2020 China Land Cover Dataset (CLCD v01; 30 m resolution) [36]. The comparison assessed whether each polygon corresponded to observed built-up land, but it did not alter the GHS-UCDB boundaries. ArcGIS 10.6 was used for spatial comparison and processing, with coordinate reference systems checked and harmonized to ensure spatial alignment. We retained urban-centre polygons larger than 10 km^2 and further restricted the sample to units with valid observations in all four assessment years, yielding 1605 analytical units. Because GHS-UCDB urban centres are defined independently of

administrative boundaries, multiple spatially separate urban centres may occur within the same administrative city. We applied the 2020 urban-centre boundaries consistently across all four assessment years, ensuring that UTCI comparisons were based on identical spatial extents rather than changing urban boundaries. The selection procedure and spatial definition of the analytical units are illustrated in Figure 2.

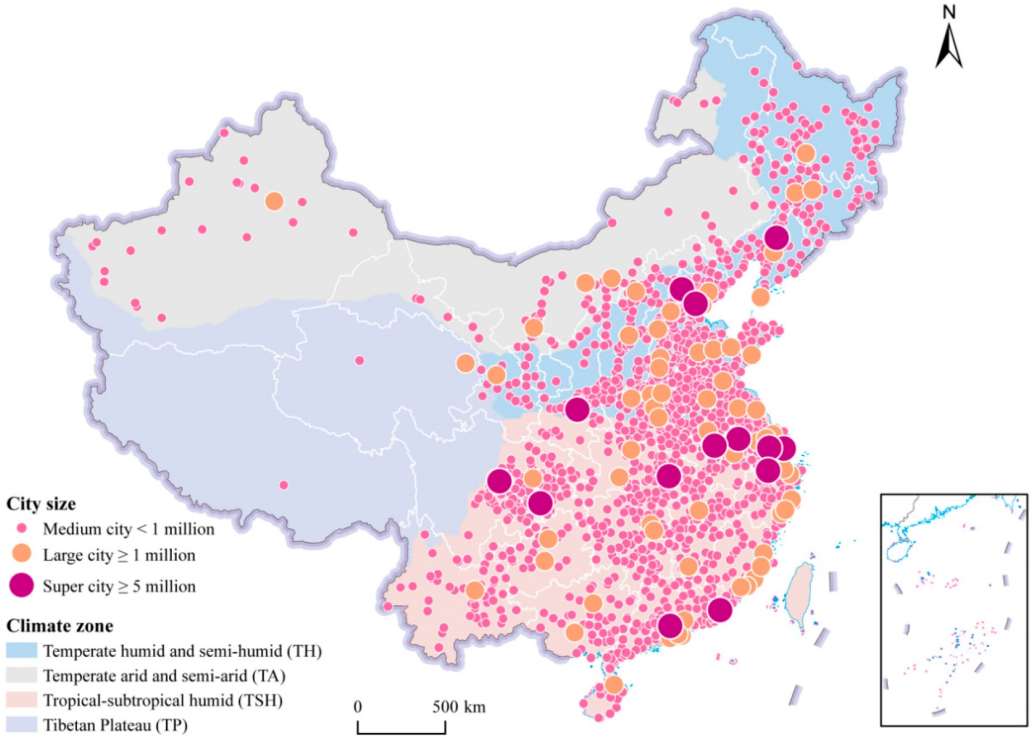

Figure 1. Spatial distribution of the 1605 GHS-UCDB urban centres included in the analysis. Points represent the centroids of urban-centre polygons used for visualization.

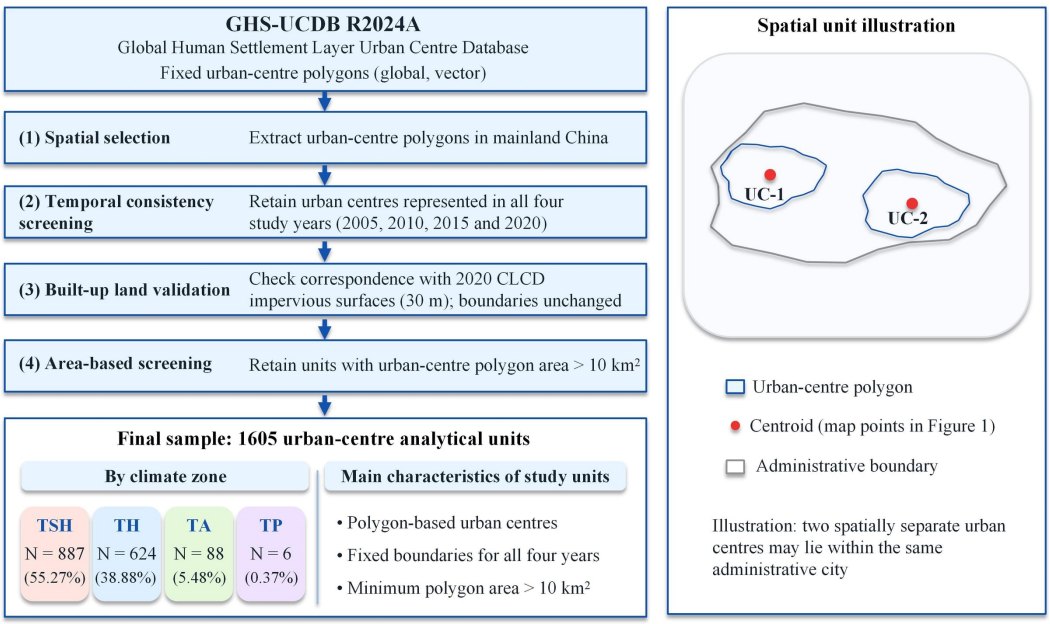

Figure 2. Selection procedure and spatial definition of the 1605 GHS-UCDB urban-centre analytical units.

2.2. Data Sources

Monthly Universal Thermal Climate Index (UTCI) estimates were obtained from GloUTCI-M, a global dataset providing UTCI estimates at a spatial resolution of 1 km and a monthly temporal resolution for 2000–2022 [37]. UTCI is a human thermal stress index that integrates the combined effects of air temperature, mean radiant temperature, wind speed, and atmospheric humidity. The GloUTCI-M was developed using UTCI reference values derived from meteorological observations and radiative information. A CatBoost machine-learning model was then used to generate spatial UTCI estimates from remotely sensed and geographical covariates, including land surface temperature, vegetation, land cover, nighttime lights, and topography. Thus, the UTCI values used in this study were obtained directly from an established gridded product rather than independently calculated from the original meteorological variables.

Four assessment years (2005, 2010, 2015, and 2020) were selected at five-year intervals to examine changes in summer thermal conditions while maintaining temporal consistency with the multi-source urban environmental datasets. For each year, monthly UTCI estimates for June, July, and August were extracted and averaged to obtain summer UTCI values. These values were then spatially averaged across all valid 1 km pixels within each urban-centre polygon using the fixed 2020 GHS-UCDB boundaries. This procedure yielded one mean summer UTCI estimate for each of the 1605 urban centres in each assessment year.

We assembled explanatory variables from public geospatial datasets to represent complementary dimensions of the urban environment (Table 1). The underlying geospatial datasets were primarily obtained through Google Earth Engine (GEE). Land-cover data were obtained from the 30 m CLCD, which includes nine classes: cropland, forest, shrubland, grassland, water, snow and ice, barren land, impervious surfaces, and wetlands. These data were used to characterize landscape composition and configuration within the study areas. MODIS products supplied the normalized difference vegetation index (NDVI), modified normalized difference water index (MNDWI), normalized difference built-up index (NDBI), surface albedo (Alb), and potential evapotranspiration (ET). The Global Human Settlement Layer (GHSL) provided built-up surface area (BS), built-up volume (BV), and population density (POP), while building height (BH) was calculated as the ratio of built-up volume to built-up surface area (BV/BS). Nighttime light (NTL) was used as a proxy for urban activity and development intensity, while TerraClimate and SRTM provided regional climate and topographic data, respectively.

Dataset-specific preprocessing and quality assurance procedures were applied to the geospatial products used in this study. Dataset-specific preprocessing and quality assurance (QA) procedures were applied to minimize the influence of cloud contamination and low-quality observations in the MODIS products. Specifically, for surface reflectance data, the StateQA band was used to identify and mask pixels affected by clouds and cloud shadows before calculating NDVI, MNDWI, and NDBI. For the albedo product, the BRDF_Albedo_Band_Mandatory_Quality_shortwave band was used to retain high-quality shortwave albedo retrievals. The remaining valid observations were temporally composited over June-August of each assessment year. The resulting explanatory variables were extracted or aggregated within the fixed urban-centre boundaries, despite differences in the spatial resolutions of the source datasets.

Table 1. Data sources used in this study.

Data Category	Spatial Resolution	Temporal Coverage	Description	Dataset or Product
Universal Thermal Climate Index	1000 m	Monthly (June-August; 2005, 2010, 2015, and 2020)	Human thermal stress	GloUTCI-M
Land cover	30 m	2005, 2010, 2015, 2020	Land-cover classification	CLCD_v01
Surface biophysical variables	500 m	Monthly (June-August; 2005, 2010, 2015, and 2020)	Vegetation, water, built-up, and surface-energy indicators	MODIS (MOD13A2, MCD43A3, MOD16A2GF)
Urban morphology and population	100 m	2005, 2010, 2015, 2020	Three-dimensional urban structure and population distribution	GHSL (BUILT-S, BUILT-V, POP)
Socioeconomic activity	500 m	2005, 2010, 2015, 2020	Proxy for anthropogenic activity	Harmonized DMSP and VIIRS nighttime-light data
Climate variables	~4.6 km	Monthly (June–August; 2005, 2010, 2015, and 2020)	Regional hydroclimatic conditions	TerraClimate
Topography	30 m	Static	Terrain characteristics	SRTM DEM
Geographic information	Not applicable	Static	Latitude of each urban-centre centroid	Urban centroid

2.3. Variables

2.3.1. Universal Thermal Climate Index

Mean summer UTCI was used as the response variable to characterize outdoor thermal stress within each urban centre, with higher values indicating greater heat stress under the summer conditions examined.

2.3.2. Candidate Explanatory Variables

We organized the candidate explanatory variables into six groups: landscape composition, landscape pattern, surface biophysical characteristics, urban morphology, socioeconomic conditions, and geographical and climatic background. This classification distinguishes built-environment characteristics related to land cover, surface properties, urban form, and development activity from broader geographical and climatic background conditions. The characteristics of the underlying datasets, including their spatial and temporal resolutions, are summarized in Table 1, while the data sources, calculation formulas, units, and definitions of individual explanatory variables are provided in Table 2. All variables were aggregated to the urban-centre scale using consistent spatial boundaries.

Table 2. Candidate explanatory variables included in this study.

Category	Variable and Abbreviation	Data Source	Formula	Range or Unit	Description
Geography and climate	DEM	SRTM DEM	_	m	Mean elevation within each urban-centre boundary
	Lat	Urban centroid	_	°	Latitude of the urban-centre centroid
	ET	MODIS	_	mm	Mean summer (June–August) potential evapotranspiration

Table 2. *Cont.*

Category	Variable and Abbreviation	Data Source	Formula	Range or Unit	Description
Geography and climate	Pre	TerraClimate	–	mm	Total summer (June–August) precipitation
	Wind		–	m/s	Mean summer (June–August) near-surface wind speed
Surface biophysical	NDVI	MODIS	$\frac{NIR-R}{NIR+R}$	(−1,1)	Mean summer (June–August) vegetation greenness
	MNDWI		$\frac{G-SWIR}{G+SWIR}$	(−1,1)	Mean summer (June–August) surface-water signal
	NDBI		$\frac{SWIR-NIR}{SWIR+NIR}$	(−1,1)	Mean summer (June–August) built-up intensity
Urban morphology	BS	GHSL	–	m^2	Total built-up surface area
	BV		–	m^3	Total built-up volume
	BH		$\frac{BV}{BS}$	m	Proxy for mean building height, calculated as built-up volume divided by built-up surface area
	Alb	MODIS	–	–	Mean summer (June–August) surface albedo
Landscape composition	ImP	CLCD	$\frac{A_{imp}}{A_{urban}}$	(0,1)	Proportion of impervious surface
	NTreeP		$\frac{A_{ntree}}{A_{urban}}$	(0,1)	Proportion of non-tree vegetation
	TreeP		$\frac{A_{tree}}{A_{urban}}$	(0,1)	Proportion of tree vegetation
	VegP		$\frac{A_{veg}}{A_{urban}}$	(0,1)	Proportion of total vegetation
	WaterP		$\frac{A_{wat}}{A_{urban}}$	(0,1)	Proportion of open water
Landscape pattern	ED	CLCD	$\frac{E}{A}$	m/ha	Total edge length of ecological patches per hectare
	PD		$\frac{N}{A} * 100$	N/100 ha	Number of ecological patches per 100 ha
	LPI		$\frac{max(A_i)}{A} * 100$	%	Percentage of the largest ecological patch
	LSI		$\frac{E_i}{min(E_i)}$	≥1	Degree of patch shape irregularity
Social and economic	POP	GHSL	–	people/ha	Mean population density
	NTL	Harmonized DMSP and VIIRS nighttime-light data	–	–	Proxy for socioeconomic activity based on mean nighttime light intensity

Notes: The symbols in the formulas are defined as follows. A_{urban} denotes the total area enclosed by the urban-centre boundary. A_{imp}, A_{ntree}, A_{tree}, A_{veg}, and A_{wat} refer, respectively, to the areas covered by impervious surface, non-tree vegetation, tree vegetation, total vegetation, and open water. For the landscape metrics, A is the total landscape area, A_i is the area of the i_{th} ecological patch, and $max(A_i)$ denotes the area of the largest patch. N represents the total number of ecological patches, whereas E is the sum of their edge lengths. $min(E_i)$ refers to the minimum perimeter possible for a patch with area A_i. *NIR*, *R*, *G*, and *SWIR* denote reflectance in the near-infrared, red, green, and short-wave infrared bands, respectively.

Landscape composition captured the share of each land-cover class within an urban-centre boundary. We calculated the proportions of open water (WaterP), impervious surface (ImP), total vegetation (VegP), tree vegetation (TreeP), and non-tree vegetation (NTreeP).

Together, these variables characterize the composition of vegetated, water-covered, and impervious surfaces within each urban centre.

Landscape pattern captured the spatial configuration of ecological land. Based on the 30 m CLCD, cropland, forest, shrubland, grassland, water bodies, and wetlands were reclassified into a single ecological land category. Four landscape-level metrics, including edge density (ED), patch density (PD), largest patch index (LPI), and landscape shape index (LSI), were calculated for each urban-centre polygon using the landscapemetrics package in R. These metrics quantify the density of ecological land edges and patches, the dominance of the largest patch, and landscape shape complexity.

NDVI, MNDWI, and NDBI represented surface biophysical characteristics. These satellite-derived indices characterize vegetation greenness, water-related spectral characteristics, and built-up surface characteristics, respectively.

BS, BV, BH, and Alb represented urban morphology. BS and BV measure the extent and three-dimensional volume of development, while BH approximates mean building height. Alb describes surface reflectivity. Together, these variables capture urban characteristics associated with radiation exchange, heat storage, and airflow.

POP and NTL represented socioeconomic conditions. POP measures resident concentration, while mean NTL intensity serves as a proxy for urban activity and development.

Elevation (DEM), potential evapotranspiration (ET), precipitation (Pre), wind speed (Wind), and latitude (Lat) represented geographical and climatic background. These variables represent differences in topography, geographical location, and regional hydroclimatic conditions.

2.4. Analytical Methods

2.4.1. Analytical Framework

The analytical framework integrated four assessment years of UTCI data with national and climate-zone-specific analyses of built-environment associations (Figure 3). We first harmonized all source datasets into a common urban-centre database and grouped the explanatory variables into six dimensions. After screening for multicollinearity and redundancy, we described summer UTCI in 2005, 2010, 2015, and 2020 and compared four predictive algorithms. We then interpreted the selected Random Forest models with SHAP values, locally weighted scatterplot smoothing (LOWESS), and two-dimensional partial dependence plots (2D PDPs). These methods quantified variable importance and characterized nonlinear marginal and pairwise responses.

2.4.2. Multicollinearity and Redundancy Analysis

We assessed multicollinearity and redundancy using variance inflation factors (VIFs) and Pearson correlations [38]. A variable was removed iteratively only when its VIF exceeded 10 and its pairwise absolute correlation coefficient exceeded 0.80. This procedure removed NTreeP, BS, MNDWI, VegP, and LPI, leaving 18 variables for modelling (Supplementary Material S1). The same screening criteria were applied consistently across all four assessment years (2005, 2010, 2015, and 2020) and all three spatial scales (national, TSH, and TH) to ensure methodological consistency and comparability across years and regions.

2.4.3. Model Comparison and Selection

We compared linear regression (LR), Random Forest (RF), Extreme Gradient Boosting (XGBoost), and the Light Gradient Boosting Machine (LightGBM). At each time point, we randomly divided observations into training and test sets in an 80:20 ratio using a fixed seed of 42. Within the training set, randomized search evaluated 30 hyperparameter

combinations by five-fold cross-validation. The folds were shuffled with the same seed, and the coefficient of determination (R^2) served as the optimization metric.

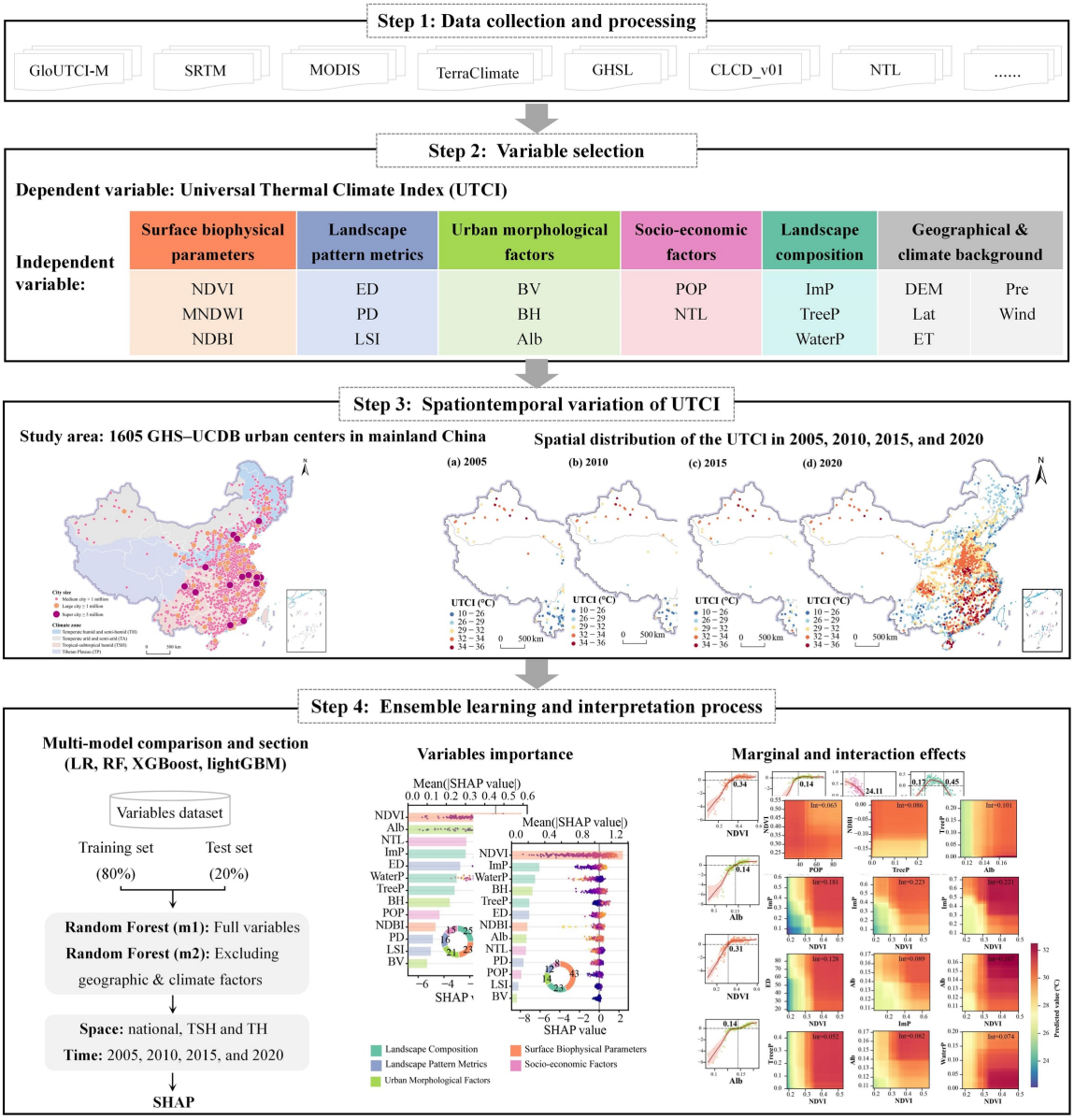

Figure 3. Workflow of the analytical framework.

The main hyperparameter candidates covered 200–600 trees for all three ensemble models; maximum depths of 10, 20, 30, or no limit for RF; learning rates of 0.01–0.20 and maximum depths of 3–9 for XGBoost; and learning rates of 0.01–0.20 and leaf counts of 15–127 for LightGBM. Additional model-specific parameters, including minimum node size and sample- and feature-subsampling parameters, were also tuned where applicable. Optimized models were evaluated on the held-out test set using R^2, root mean square error (RMSE), and mean absolute error (MAE).

At the national scale, RF achieved the highest R^2 values in 2005 (0.762), 2010 (0.655), and 2015 (0.592), together with the lowest RMSE and MAE values in these three years (Supplementary Material S2). As an ensemble of randomized decision trees, RF can capture nonlinear relationships and predictor interactions without requiring a predefined functional form [39]. Although alternative ensemble algorithms may perform better in certain settings, RF was selected as the common modelling algorithm for subsequent analyses at both

national and climate-zone scales based on its overall predictive performance and suitability for examining predictor importance, nonlinear responses, and interactions. This consistent modelling framework also facilitated comparisons across regions and assessment years.

We fitted two predictor specifications to separate broad environmental context from urban characteristics. Model m1 included all retained variables, including geographical and climatic covariates. Model m2 retained only built-environment variables. Supplementary Material S3 compares their predictive performance. The main interpretation focused on m2 to examine the relative importance and nonlinear associations of built-environment predictors. These results characterize associations within the retained predictor set rather than the complete predictive structure or causal determinants of UTCI.

Using m2, we fitted separate RF models for TSH and TH. These regional models enabled comparison within the two humid zones that had sufficient samples. TA and TP remained in the descriptive UTCI analysis but were excluded from regional modelling. Their smaller samples, especially the six TP urban centres, raised concerns about model stability. The optimized RF hyperparameter configurations and corresponding predictive performance of the m2 models across the three study regions and four assessment years are provided in Tables S5 and S6.

2.4.4. SHAP-Based Model Interpretation and Interaction Analysis

We interpreted RF predictions using SHAP values [30]. SHAP decomposes each prediction into contributions from individual variables. Positive and negative values indicate contributions above and below the model's expected prediction, respectively. Mean absolute SHAP values from the training data ranked global feature importance. Relative SHAP importance (%) was calculated as each predictor's mean absolute SHAP value divided by the sum of mean absolute SHAP values for all 13 predictors within the same region–year model, multiplied by 100. SHAP values from the held-out test set supported the marginal-response and pairwise interaction analyses. To assess the consistency of predictor importance across model specifications, we compared the rankings of the 13 shared built-environment predictors between m1 and m2.

We calculated pairwise SHAP interaction values for the test observations. SHAP interaction values quantify the contributions of pairwise feature interactions to model predictions within the Shapley-value framework [40]. For each region–year model, the four variables with the highest training-set mean absolute SHAP values were selected, yielding six candidate interaction pairs. Interaction strength (Int) was quantified as the mean absolute pairwise SHAP interaction value across test observations. Absolute values were used to avoid cancellation between positive and negative interaction contributions. The six candidate pairs were ranked in descending order of Int, and the three strongest pairs were visualized using 2D PDPs based on the training data. A higher Int indicates a greater average interaction contribution to model predictions among the evaluated candidate pairs. However, these values characterize interactions within the fitted model and do not, by themselves, establish statistical significance or causal relationships.

2.4.5. Nonlinear Response Analysis and Zero-Crossing Identification

Nonlinear marginal-response analysis focused on the four variables with the highest training-set mean absolute SHAP values in each model. We fitted LOWESS curves to the relationships between predictor values and their corresponding SHAP values in the test set, using a smoothing fraction of 0.4 and no robustness iterations to characterize nonlinear associations without imposing a predefined functional form [41]. To assess the resampling variability of the fitted LOWESS curves, pointwise 95% bootstrap intervals were estimated using the 2.5th and 97.5th percentiles of the fitted values obtained from

100 bootstrap resamples [42]. These intervals reflect variability in the fitted LOWESS curves under resampling and should not be interpreted as confidence intervals for causal effects or formally validated thresholds.

We defined an estimated zero-crossing point as the intersection of a fitted LOWESS curve and the SHAP = 0 reference line. When adjacent fitted points had opposite signs, we estimated the crossing by linear interpolation and retained every distinct crossing. These points indicate where fitted SHAP contributions change sign relative to the model's expected prediction; they do not establish statistical thresholds or causal breakpoints.

3. Results

3.1. UTCI Across Time and Climate Zones

Figure 4 presents the spatial distribution of mean summer UTCI values across the four assessment years and compares UTCI distributions among population-size classes and climate zones. According to the standard UTCI classification, values of 9–26 °C indicate no thermal stress, 26–32 °C moderate heat stress, and 32–38 °C strong heat stress [15]. To improve spatial differentiation, the maps further subdivided the higher UTCI ranges into 26–29, 29–32, 32–34, and 34–36 °C, while values below 26 °C were grouped into a single class.

A broadly similar spatial pattern was observed across the four assessment years (Figure 4a–d). Values of 29–32 °C formed a broad band across central and eastern China. Higher values of 32–36 °C clustered along the middle and lower Yangtze River, in the Pearl River Delta, along the southeastern coast, and in the Sichuan Basin. Values below 29 °C occurred mainly in Northeast China and the high-elevation areas of southwestern China.

Across all sampled urban centres, mean UTCI increased from 29.61 °C in 2005 to 29.99 °C in 2010. It declined slightly to 29.92 °C in 2015 before reaching 30.43 °C in 2020. The mean UTCI difference between 2005 and 2020 was 0.82 °C (SD = 2.72 °C; 95% CI: 0.70–0.97 °C), and the difference was statistically significant (paired t-test, $p < 0.001$). However, these four assessment years do not establish a continuous annual trend. At the urban-centre level, 73.02% recorded a higher value in 2020 than in 2005. The number of centres in the 34–36 °C class increased from 11 to 129. The 32–34 °C class grew from 351 to 514, while the 29–32 °C class contracted from 745 to 515. These changes indicate a shift toward higher UTCI classes between 2005 and 2020. The spatial distribution of city-level UTCI differences (Figure 5) further revealed considerable geographical heterogeneity, with both positive and negative changes across the study area rather than a spatially uniform increase.

UTCI distributions also differed by population-size class (Figure 4e). Supercities had the highest values at every time point. Medium cities showed a broader distribution and a longer lower tail. In 2020, the central portions of all three distributions were higher than those in 2005. The endpoint increase was therefore not confined to a single population-size class.

Climate zones separated the observations more clearly (Figure 4f). TSH consistently had the highest mean UTCI, followed by TH, while TA and TP remained cooler. Between 2005 and 2020, mean UTCI increased by 1.08 °C in TSH (SD = 3.49 °C; 95% CI: 0.85–1.28 °C) and 0.64 °C in TH (SD = 1.10 °C; 95% CI: 0.56–0.73 °C). The difference in urban-centre UTCI changes between the two zones was statistically significant (Welch's t-test, $p < 0.001$). In contrast, mean UTCI declined slightly in TA (−0.35 °C) and TP (−0.16 °C). The endpoint increase was therefore concentrated in the two humid zones.

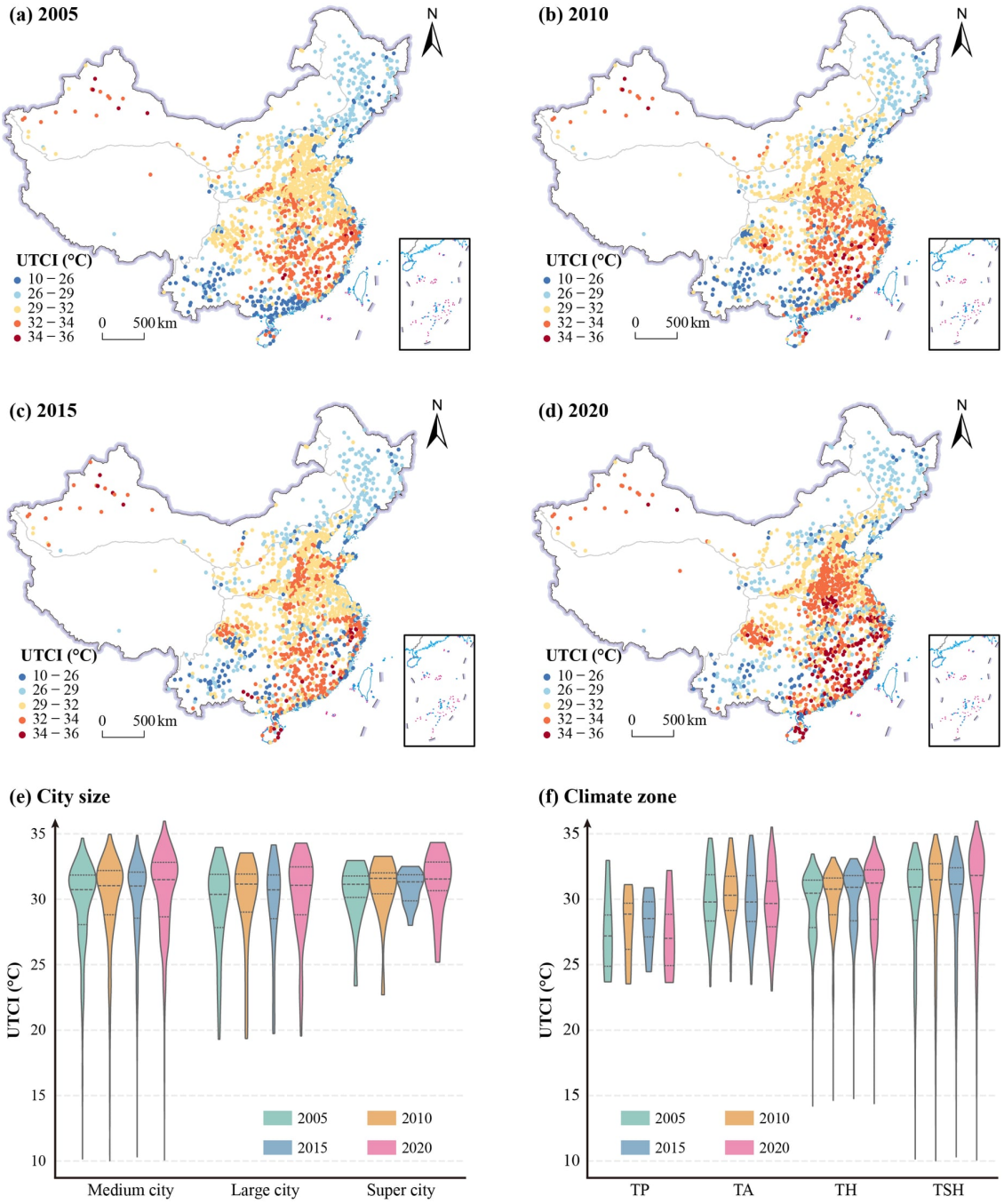

Figure 4. Mean summer UTCIs across the sampled urban centres in 2005, 2010, 2015, and 2020. Panels (**a**–**d**) map UTCI; panels (**e**,**f**) compare distributions by population-size class and climate zone.

3.2. Built-Environment Importance Varies by Scale and Climate

The predictive performance of the m2 was evaluated across the three study regions and four assessment years (Table S6). The test R^2 values ranged from 0.413 to 0.525 nationally, 0.421 to 0.555 in TSH, and 0.573 to 0.628 in TH. The corresponding RMSE ranges were 2.354–2.665, 3.427–3.887, and 1.507–1.815 °C, while the MAE ranges were 1.687–1.930, 2.272–2.673, and 0.997–1.287 °C, respectively. Subsequent interpretation focused on the m2 model to characterize the associations between built-environment factors and UTCI.

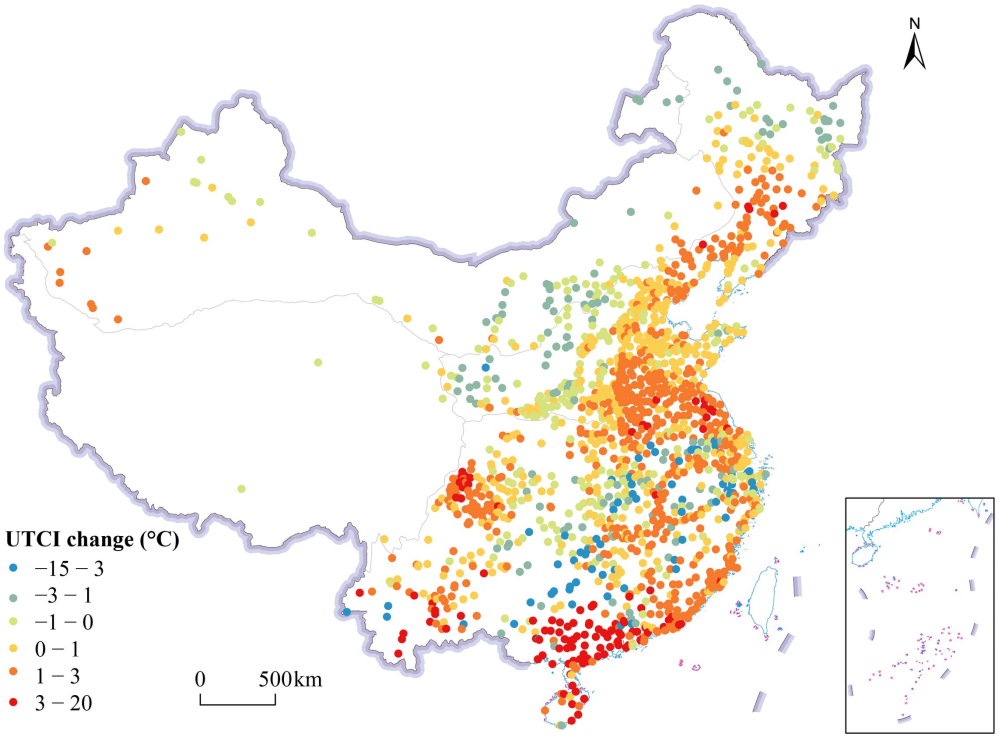

Figure 5. Spatial distribution of changes in mean summer UTCI across 1605 urban centres in China between 2005 and 2020.

Figure 6 compares the relative importance of built-environment variables in the national, TSH, and TH m2 models across the four assessment years. Table S3–S5 reports the corresponding relative SHAP importance (%) and rankings of all 13 predictors for each region–year model.

The national importance structure differed considerably among the four assessment years (Figure 6). Landscape composition ranked first in 2005 and accounted for 25% of total importance. Surface biophysical characteristics led in 2010 and 2020, while urban morphology led in 2015 with 37%. Landscape pattern rose from 16% in 2005 to 25% in 2020 and ranked second at the final time point. In contrast, the socioeconomic share fell from 15% to 7%. At the variable level, NDVI ranked first in 2005 and 2010, accounting for 18.6% and 21.9% of total SHAP importance, respectively, whereas Alb ranked first in 2015 and 2020, with corresponding shares of 29.4% and 18.4%. ED remained among the three leading variables after 2010, and NDBI entered the top four in both later years. In contrast, NTL ranked third in 2005 and fourth in 2010 but occupied lower positions in 2015 and 2020.

The TSH models showed greater consistency in the relative importance rankings of leading predictors across the four assessment years. Surface biophysical characteristics ranked first in 2005, 2010, and 2020, while landscape composition led in 2015. Together, these groups contributed more than 60% of total importance every year. NDVI ranked first throughout, accounting for 37.5%, 36.1%, 22.6%, and 33.9% of total SHAP importance in 2005, 2010, 2015, and 2020, respectively. ImP consistently ranked second, with its relative importance increasing from 9.3% in 2005 to 21.0% in 2020. Alb ranked eighth in 2005 and 2010 but third in 2015 and 2020. BH fell from fourth in 2005 to last in 2020. TreeP remained in the top four through 2015 before dropping to ninth, while WaterP stayed in the top five at all four time points.

The TH models exhibited greater differences in predictor importance across the four assessment years than the TSH models. Urban morphology ranked first in 2005, 2010, and 2020, while landscape composition led in 2015. Landscape pattern increased from 14%

in 2005 to 24% in 2020, whereas surface biophysical characteristics declined from 18% to 10%. The socioeconomic share also fell after 2010. At the individual-variable level, Alb ranked first in 2005, 2010, and 2020, accounting for 22.1%, 21.9%, and 25.4% of total SHAP importance, respectively. TreeP ranked first in 2015 (19.1%) and second in 2020 (19.6%), while LSI ranked fifth in 2010 and third in 2020. POP ranked second in 2005 and 2010 but sixth in 2020. By contrast, NDBI occupied a relatively low rank in the earlier assessment years but ranked second in 2015 and fourth in 2020.

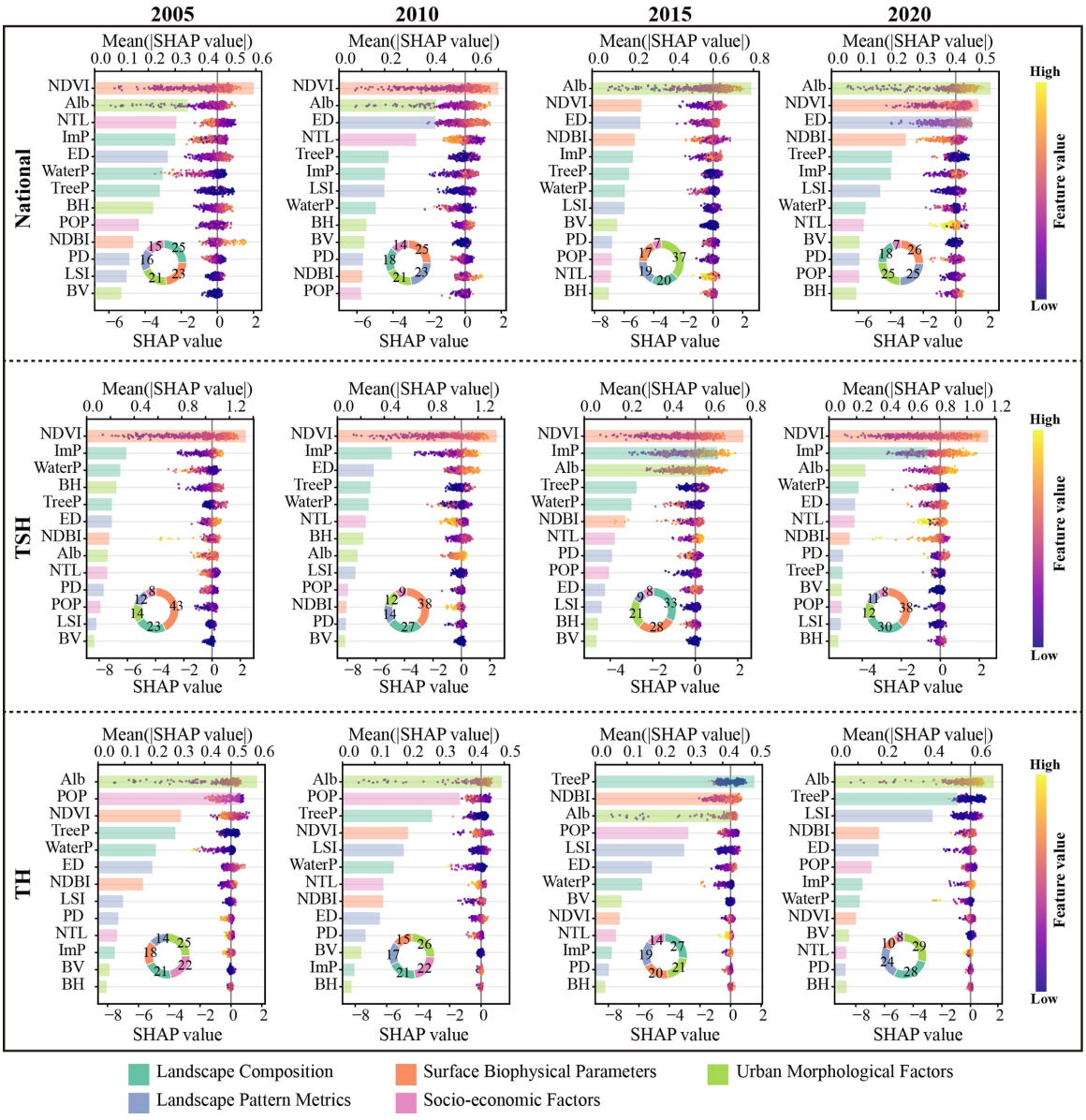

Figure 6. Relative importance of built-environment variables in the national, TSH, and TH models at four time points.

3.3. Nonlinear Marginal Responses Differ Across Models

Figure 7 shows marginal SHAP response curves for the leading predictors in each national, TSH, and TH model. The curves followed five recurring forms: increase–plateau, monotonic increase, monotonic decrease, inverted U, and hump-shaped. Several variables retained a general response form, but curve shape and zero-crossing location often changed across years or modelling regions.

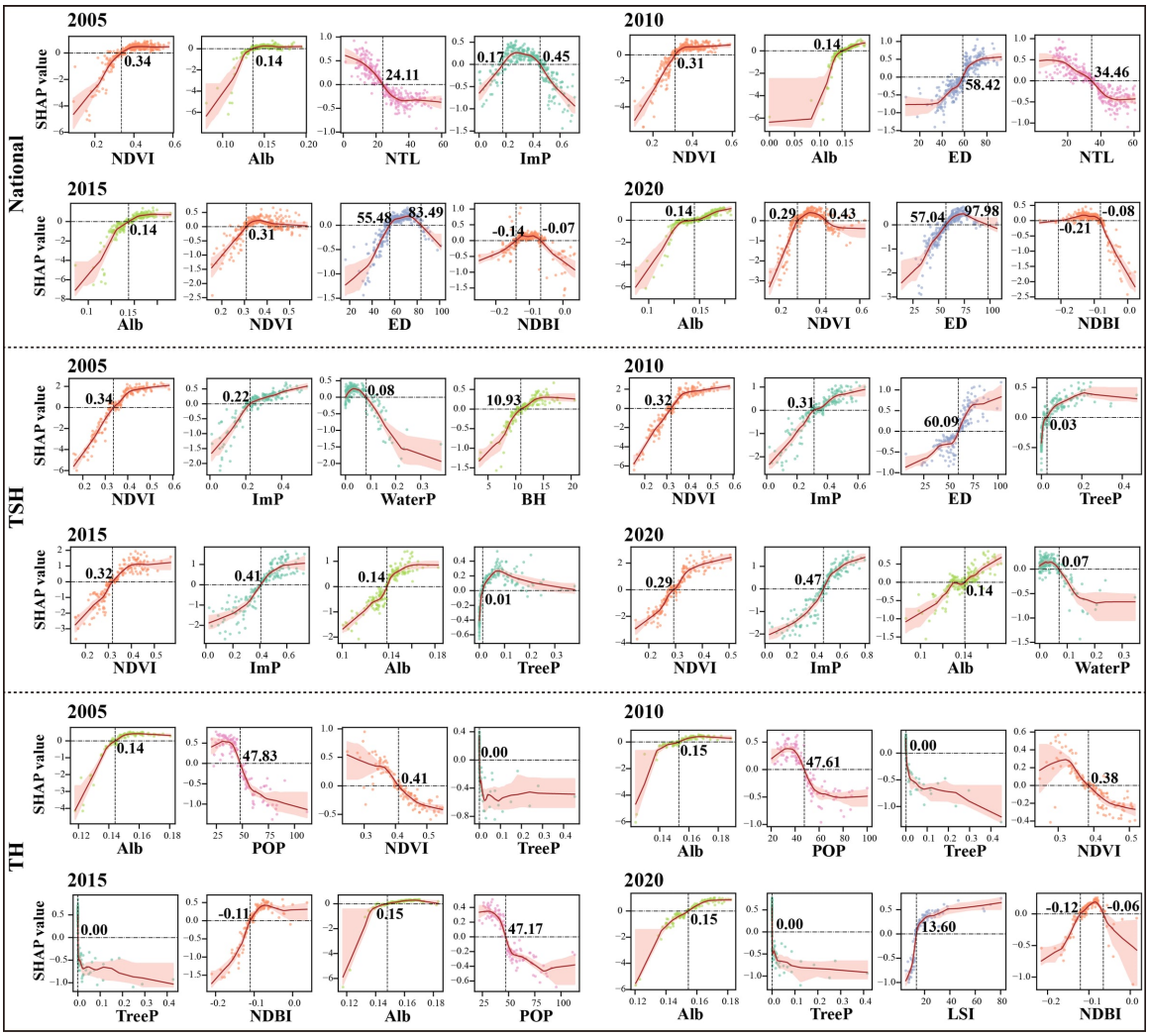

Figure 7. Marginal SHAP response curves for leading built-environment variables in the national, TSH, and TH models.

Nationally, NDVI followed an increase–plateau response in 2005 and 2010, with approximate transitions at 0.34 and 0.31. In contrast, NDVI exhibited an inverted-U response in 2015 and 2020. In 2020, positive SHAP values occurred mainly between approximately 0.29 and 0.43. Alb showed an increasing response across all four assessment years, with estimated SHAP zero-crossing points near 0.14. ED followed an increase–plateau response in 2010, with a transition near 58. In 2015 and 2020, ED exhibited an inverted-U response, with positive ranges of approximately 55–83 and 57–98, respectively. NTL exhibited monotonically decreasing SHAP responses in 2005 and 2010, with estimated zero-crossing points near 24 and 34, respectively. NDBI entered the leading set in 2015 and 2020 and followed an inverted U, with positive ranges of approximately −0.14 to −0.07 and −0.21 to −0.08.

The TSH models showed greater consistency in the response patterns of leading predictors across the four assessment years. NDVI followed an increase–plateau response every year, while its approximate transition moved from 0.34 in 2005 to 0.29 in 2020. ImP exhibited a positive nonlinear response, with an estimated SHAP zero-crossing point of approximately 0.22 in 2005 and 0.47 in 2020. Alb entered the leading set in 2015, exhibiting an increase–plateau response in 2015 and a monotonically increasing response in 2020. Its estimated SHAP zero-crossing point was near 0.14 in both years. WaterP was hump-shaped in 2005 and 2020, peaking near 0.08 and 0.07 before declining. TreeP changed from an

increase–plateau response in 2010 to hump-shaped responses in 2015 and 2020. Its SHAP zero-crossing points occurred near 0.03, 0.01, and 0.07.

The TH curves varied more over time. Alb consistently followed an increase–plateau pattern, with transitions near 0.14–0.15. In 2005, 2010, and 2015, the POP response curves changed direction near 47, with SHAP values generally declining at higher POP levels. NDVI exhibited a monotonically decreasing response in 2005 and a hump-shaped response in 2010, with the latter peaking near 0.38. TreeP remained a leading variable from 2005 through 2015. Its responses were concentrated at low cover, and SHAP values generally declined as cover increased. NDBI entered the leading set in 2015. It showed an increase–plateau response with an estimated SHAP zero-crossing point near −0.11 in 2015. In 2020, NDBI exhibited an inverted-U response, with positive SHAP values occurring approximately between −0.12 and −0.06.

These curves indicate nonlinear and context-dependent associations between built-environment predictors and UTCI, with estimated zero-crossing points and response ranges varying across models.

3.4. Leading Pairwise Interactions Vary by Year and Climate

Figures 8 and 9 present the three strongest interaction pairs (Int) selected from the six candidate pairs formed by the four highest-ranked predictors in each region–year model, together with their 2D PDPs. National models were characterized by NDVI-related leading pairs in 2005 and 2010, whereas Alb-related pairs were more prominent in 2015 and 2020. NDVI appeared in the leading TSH pair in all four assessment years, while the leading TH pairs differed more markedly among the assessed years. These patterns describe joint model responses rather than significance-tested or causal interactions.

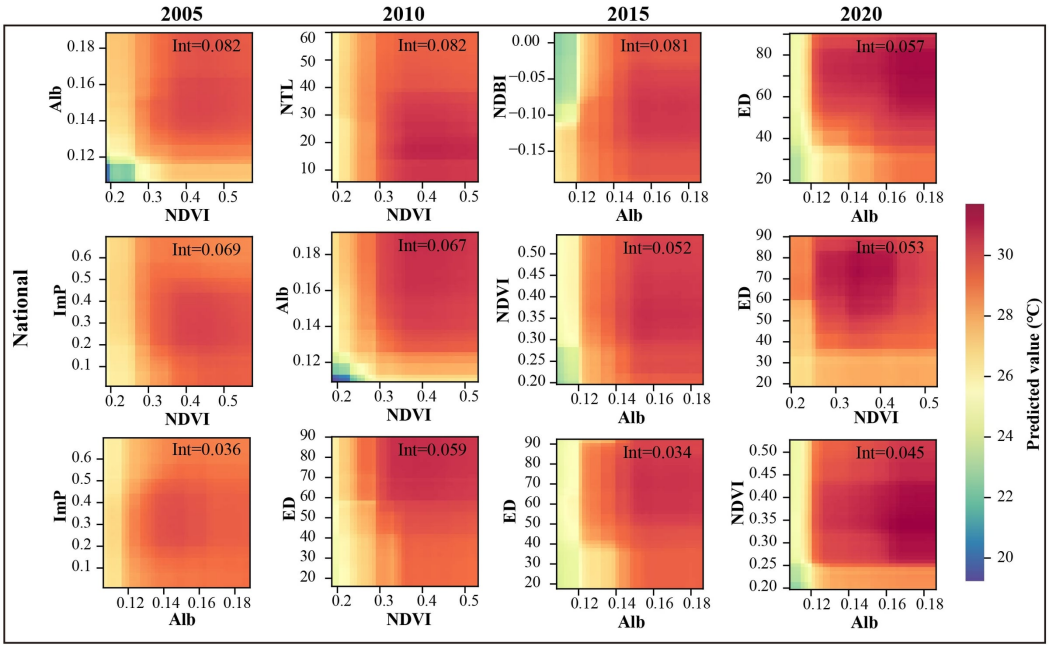

Figure 8. Two-dimensional partial dependence surfaces for the strongest variable pairs in the national models.

At the national scale, NDVI-Alb ranked first in 2005 (Int = 0.082), followed by NDVI-NTL as the leading pair in 2010 (Int = 0.082). Alb-NDBI ranked first in 2015 (Int = 0.081), whereas Alb-ED ranked first in 2020 (Int = 0.057).

In 2005 and 2010, response surfaces involving NDVI changed near 0.30. Predicted UTCI was lower below this value and shifted upward as NDVI increased. Within the higher-NDVI

range, Alb above approximately 0.12 and ED above approximately 60 corresponded to higher predicted UTCI.

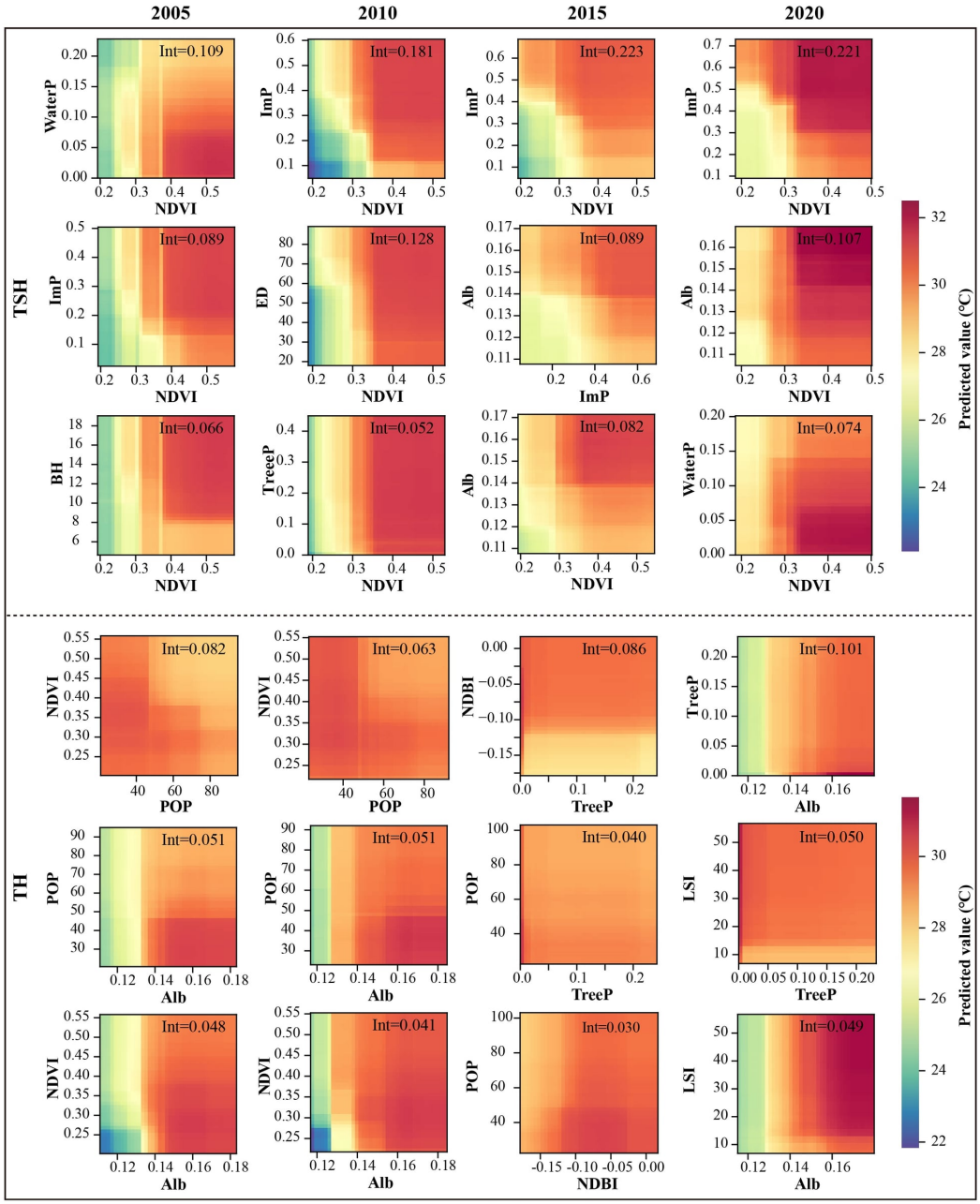

Figure 9. Two-dimensional partial dependence surfaces for the strongest variable pairs in the TSH and TH models.

In 2015 and 2020, Alb-related pairs were more prominent. In the Alb-NDBI surface, predicted UTCI was generally lower when Alb was below approximately 0.12. Above this value, predictions increased and reached relatively high levels when NDBI ranged from approximately −0.12 to −0.08. The Alb-ED surface behaved differently under low-Alb conditions, where predicted UTCI generally rose with ED. Above the same Alb transition, predictions remained higher and reached their largest values when ED exceeded approximately 40. The Alb-NDVI surface showed a similar Alb transition, with clearer variation along NDVI above approximately 0.12.

Within TSH, NDVI occurred in the leading interaction pair at every time point (Figure 9). NDVI–WaterP ranked first in 2005 (Int = 0.109). NDVI-ImP ranked first in

2010, 2015, and 2020, with interaction strengths of 0.181, 0.223, and 0.221, respectively. The interaction was stronger in 2015 and 2020 than in 2010.

In 2005 and 2010, NDVI-related surfaces changed near 0.30, and predicted UTCI shifted upward above this value. Within the higher-NDVI range, WaterP below approximately 0.08 corresponded to higher predictions. The NDVI-ImP and NDVI-ED surfaces followed similar patterns. ImP above approximately 0.20 and ED above approximately 30 corresponded to higher predictions when NDVI was relatively high. In the NDVI-BH surface, BH above approximately 8 corresponded to higher predictions when NDVI exceeded approximately 0.36.

NDVI-ImP remained the leading TSH pair in 2015 and 2020. When NDVI exceeded approximately 0.30, predicted UTCI was higher with ImP above 0.40 in 2015 and above 0.30 in 2020. The ImP-Alb and NDVI-Alb surfaces also changed along the Alb dimension. Predictions shifted upward above an Alb value of approximately 0.14. This increase was clearest when ImP exceeded 0.40 or NDVI exceeded 0.30. The NDVI–WaterP surface showed a pattern similar to that observed in 2005, with lower WaterP associated with higher predicted UTCI at relatively high NDVI levels.

In TH, NDVIPOP remained the leading interaction pair in 2005 and 2010, with interaction strengths of 0.082 and 0.063, respectively (Figure 9). The leading pair shifted to TreePNDBI in 2015 (Int = 0.086) and AlbTreeP in 2020 (Int = 0.101).

In 2005 and 2010, the three strongest TH pairs were NDVI-POP, Alb-POP, and Alb-NDVI, although their order varied. NDVI-POP ranked first in both years. Predicted UTCI was higher when POP was below approximately 50 and declined slightly beyond that range. The Alb-POP and Alb-NDVI surfaces both changed near Alb = 0.14. Predictions shifted upward above this value, with clearer variation along POP and NDVI.

The TH interaction structure differed among the four assessment years. In 2015, the TreeP–NDBI surface varied mainly along the NDBI dimension, with predicted UTCI increasing above approximately −0.12 and then levelling off. Variation along the TreeP dimension was relatively limited. TreeP-POP and NDBI-POP had weaker gradients and interaction strengths below 0.04. In 2020, Alb-TreeP ranked first. Its surface varied mainly along Alb, with predictions shifting upward above approximately 0.13. Alb-LSI showed a similar transition along the Alb dimension.

4. Discussion

4.1. Urban Thermal Stress Follows Regional Climate Gradients

Across the four assessment years, UTS exhibited a broadly consistent spatial gradient, with higher UTCI values in southern and low-elevation urban centres and lower values in northern and high-elevation areas. The endpoint increase from 2005 to 2020 was also concentrated in the humid climate zones, particularly TSH. These patterns are consistent with regional differences in air temperature, humidity, wind, radiation, elevation, and atmospheric circulation [43]. Previous UTCI-based research in Europe similarly identified pronounced geographical differences in summer thermal stress [44]. More recently, Iqbal et al. [45] reported intensifying summer-monsoon thermal stress across major urban agglomerations in eastern China. Consistent with these studies, our findings highlight the importance of climatic context in shaping human thermal exposure. However, differences in geographical coverage, temporal resolution, and study periods limit direct quantitative comparisons.

The higher national mean UTCI in 2020 than in 2005 may reflect the combined influence of climate warming and urban environmental changes [3–5,8,25,46]. Nevertheless, the four assessment years represent discrete observations rather than a continuous record, and the lower mean in 2015 may partly reflect interannual meteorological variability associated

with atmospheric circulation and monsoon conditions [47–49]. Regional differences further complicate this interpretation: TSH exhibited the highest UTCI and largest endpoint increase, TH showed a more moderate increase, and TA and TP changed relatively little. Because UTCI integrates air temperature, humidity, wind, and radiation, these contrasts may reflect differences in meteorological conditions and their modulation by regional circulation [15,38,43,50,51]. Their individual contributions, however, cannot be isolated from the present analysis.

4.2. Built-Environment Associations Differ Between Humid Climate Zones

National and regional models revealed distinct patterns of built-environment importance. NDVI ranked first nationally in 2005 and 2010, whereas Alb ranked first in 2015 and 2020. In TSH, NDVI and ImP consistently occupied the leading positions, while TH showed more varied importance rankings involving Alb, TreeP, urban morphology, and landscape configuration. These differences suggest that national rankings may not adequately represent associations within individual climate zones.

Comparisons with previous studies provide context for these findings. A global analysis of approximately 500 cities reported weaker green-space cooling capacity in tropical and subtropical regions [52], while Leng et al. [53] identified diminishing cooling returns from urban greening under changing climatic conditions. In our study, NDVI remained the highest-ranked predictor in TSH, although its association with UTCI was nonlinear. This difference may reflect the distinction between vegetation cooling effects and SHAP-based relative predictor importance, as well as differences in geographical coverage and analytical scale. Similarly, a study of 682 cities found positive relationships between impervious-surface fraction and land surface temperature, with climate-dependent variations [54], whereas our results identified a positive but nonlinear ImP-UTCI association in TSH. Wu et al. [55] further examined the spatial drivers of surface urban heat islands in eastern China and highlighted the roles of surface characteristics, including albedo and vegetation. Our findings likewise identified important albedo- and vegetation-related associations, but their relative importance varied across climate zones and assessment years. Differences in thermal indicators, spatial scales, climate-zone definitions, and modelling methods may explain these variations.

In TSH, vegetation condition and impervious development formed a relatively consistent association structure. Vegetation can influence thermal conditions through canopy shading, which reduces radiation reaching underlying surfaces, and transpiration, which contributes to latent heat exchange and alters surface-energy partitioning [56]. Under warm and humid conditions, atmospheric constraints on evaporation may influence the magnitude of vegetation-related cooling. These processes provide a plausible physical context for the nonlinear NDVI response, although the fitted SHAP relationship does not directly quantify vegetation cooling. Impervious surfaces can reduce evaporation, increase heat storage, and modify sensible and latent heat exchange [57,58], potentially contributing to higher near-surface thermal loads. The positive ImP response in TSH is consistent with these processes, while its reduced slope at higher ImP values suggests a weakening marginal model response rather than confirmed physical saturation.

The leading NDVI-ImP interaction further indicates that the modelled association between vegetation greenness and UTCI depends partly on impervious-surface coverage. Extensive impervious development may alter local heat storage, moisture availability, and surface-energy exchange, thereby modifying vegetation-related thermal responses. Conversely, vegetation may influence the thermal implications of impervious development through shading and evapotranspiration. This interaction suggests that vegetation and impervious surfaces should not be interpreted as entirely independent predictors of urban

thermal conditions. However, SHAP interaction values describe statistical dependence within the fitted model and do not establish direct physical interactions or causal mechanisms. Independent observations and process-based simulations are needed to evaluate these explanations.

In TH, the importance of TreeP and landscape configuration suggests that vegetation-related associations depend not only on coverage but also on spatial arrangement. The LSI–TreeP interaction indicates that the modelled TreeP response varies with landscape configuration. Fragmented or complex green-space patterns may influence airflow, heat dispersion, and the spatial continuity of vegetation-related cooling [59]. Nevertheless, the direction and magnitude of these processes cannot be inferred directly from the interaction values, and the findings do not establish a preferred landscape design. Surface albedo showed nonlinear associations with UTCI in both humid zones and was particularly prominent in TH. Greater surface reflectivity can reduce absorbed solar radiation and surface heating, but increased reflected shortwave radiation may also raise pedestrian radiation exposure and mean radiant temperature. Because mean radiant temperature contributes to UTCI, higher surface albedo does not necessarily correspond to lower human thermal stress [60]. This distinction between surface cooling and human thermal exposure may help explain the modelled albedo associations and highlights the importance of considering radiative processes when interpreting Alb.

Water-related associations were also context dependent. Water bodies can influence surface-energy exchange through evaporation while modifying local humidity and radiation exposure [61]. Accordingly, the nonlinear WaterP response suggests that water coverage alone may not fully characterize water-related thermal conditions, which may also depend on surrounding land cover and spatial configuration. Taken together, the nonlinear responses and interactions involving NDVI, ImP, Alb, and landscape characteristics indicate that built-environment associations with UTCI vary across climatic contexts. The identified response ranges should therefore be interpreted as fitted statistical relationships rather than confirmed physical thresholds or causal effects.

4.3. Climate-Specific Implications for Urban Adaptation

The differences among national, TSH, and TH models support climate-specific approaches to urban thermal adaptation. National results identify broad associations, whereas regional models highlight combinations of built-environment characteristics that warrant local investigation. These differences suggest that adaptation assessments should consider climatic context rather than apply uniform priorities derived from national predictor rankings.

In TSH, impervious development and vegetation warrant joint consideration. The fitted ImP response increased rapidly within a model-derived range of approximately 0.3–0.4 before weakening, while the NDVI-ImP interaction suggests that vegetation-related thermal associations vary with surrounding development intensity. These findings motivate further investigation of vegetation placement, permeable surfaces, and land-use configurations in warm–humid urban centres. The nonlinear Alb response also suggests that reflective materials should be assessed in relation to pedestrian radiation exposure rather than surface temperature alone.

In TH, tree cover, surface albedo, urban morphology, and landscape configuration may require integrated assessment. The importance of TreeP and its interactions with landscape characteristics suggests that vegetation coverage and spatial arrangement should be considered together. Albedo-related measures should also account for potential differences between surface cooling and human thermal exposure. These findings provide a basis for

evaluating combinations of urban greening, landscape configuration, and surface-material characteristics under local climatic conditions.

At the national scale, the fitted NDVI response exhibited a model-derived range around 0.30, whereas Alb and ImP showed different response patterns in the regional models. Such differences may help identify built-environment characteristics that warrant closer examination, but the fitted response ranges should not be treated as optimal intervention thresholds. Their practical relevance requires independent observations, finer-scale microclimatic analyses, and location-specific validation.

4.4. Model Robustness and Spatial Generalizability

4.4.1. Robustness of Predictor Importance

To assess the robustness of built-environment predictor importance, we compared the SHAP-based rankings of the 13 shared built-environment predictors between m1 and m2 (Table S7). The highest-ranked built-environment predictor remained unchanged in 10 of the 12 region–year comparisons. This consistency was particularly evident in the climate-zone-specific models, with NDVI ranking first in TSH across all four years and Alb ranking first in TH in three of the four years. These findings suggest relatively stable leading associations across predictor specifications. Nevertheless, SHAP rankings represent relative importance within each model and should not be interpreted as independent effects after fully controlling for geographical and climatic conditions.

Predictor-exclusion sensitivity analyses were further conducted to assess potential information overlap between the built-environment predictors and the inputs used to generate GloUTCI-M. Four specifications were considered: the baseline model containing all 13 predictors (m2); a model excluding NTL (m3); a model additionally excluding ImP, TreeP, and WaterP (m4); and a model further excluding NDVI (m5). For m2-m4, RF models were refitted across the national, TSH, and TH samples and four assessment years using 30 repeated training–test partitions. Comparisons of mean absolute SHAP values showed that NDVI generally ranked higher than Alb in TSH, whereas Alb was more important in TH; nationally, NDVI was more important in 2005 and 2010, and Alb in 2015 and 2020. These patterns remained largely unchanged under m3 and m4 (Table S9).

The additional model m5 analysis used a fixed training–test partition and the same hyperparameter optimization procedure. Among the eight predictors shared by models m2 and m5, the highest-ranked predictor remained unchanged across all 12 region–year comparisons, while exact rank agreement ranged from 50% to 100%, averaging 76% (Table S10). These findings indicate that the leading importance rankings among the retained predictors were relatively stable after excluding potentially overlapping variables. However, because NDVI was excluded from m5, this analysis cannot independently establish the robustness of NDVI importance in the baseline model.

4.4.2. Robustness of Predictor Interaction

The robustness of leading predictor interactions was assessed using 30 repeated random training–test splits and eight alternative RF hyperparameter configurations across the 12 region–year models. For each model, the six interaction pairs formed by the four highest-ranked baseline predictors were retained as fixed candidates. Stability was evaluated using mean interaction strength, empirical 2.5th-97.5th percentile intervals, and Top 1 and Top 3 ranking frequencies across repeated splits, together with Top 1 frequencies across alternative RF configurations (Table S11).

The baseline leading interaction ranked first in at least 60.0% of repeated splits and among the top three in at least 86.7% across all 12 models. It also ranked first under at least seven of the eight alternative RF configurations. Nationally, Alb-NDVI in 2005 ranked

first in all 30 repeated splits and seven RF configurations. In TSH, NDVI-ImP ranked first across all repeated splits during 2010–2020 and in at least seven RF configurations. In TH, TreeP-NDBI in 2015 and Alb-TreeP in 2020 retained their first-place rankings in 90.0% and 93.3% of repeated splits, respectively. However, the national Alb-ED interaction in 2020 ranked first in only 60.0% of repeated splits, although it remained among the top three in 86.7% of cases.

These findings generally support the stability of leading interactions within the evaluated candidate pairs. Nevertheless, some interaction rankings remained sensitive to sample partitioning, and the results should be interpreted as relatively robust model-derived associations under the tested conditions rather than universally stable or causal relationships.

4.4.3. Spatial Validation and Model Generalizability

To evaluate spatial generalizability, five-fold spatial block cross-validation was compared with random five-fold cross-validation for the m2 RF models across the national, TSH, and TH samples and four assessment years. Spatial block cross-validation was adopted to reduce potential overoptimism in model evaluation arising from spatial dependence among geographically proximate observations [62]. Because the appropriate blocking scale depends on the spatial structure of the data and the validation objective, three block sizes (150, 250, and 350 km) were examined to assess the sensitivity of model performance to spatial partitioning. A primary block size of 250 km was used, with 150 and 350 km additionally examined as smaller- and larger-scale sensitivity settings. These distances were treated as alternative validation scales rather than theoretically optimal block sizes. Urban centres within the same spatial block were assigned to the same validation fold, and hyperparameters were optimized using five-fold inner cross-validation and 30 randomized-search iterations. Residual spatial autocorrelation was assessed using global Moran's I under 4-, 8-, and 12-nearest-neighbor configurations, with significance evaluated using 999 permutations (Table S12).

Spatial block cross-validation generally yielded lower predictive performance than random cross-validation, with the difference becoming more pronounced at larger block sizes. Across the 12 region–year models, mean R^2 was 0.326 under random cross-validation, compared with 0.318, 0.281, and 0.251 for spatial block sizes of 150, 250, and 350 km, respectively. RMSE and MAE generally increased under spatial validation. Residual Moran's I remained positive and statistically significant across all validation settings ($p = 0.001$), indicating persistent residual spatial autocorrelation.

These findings suggest that random cross-validation may overestimate predictive performance for geographically separated urban centres. The reduced performance under spatial validation and persistent residual spatial autocorrelation indicate limitations in the geographical generalizability of the models. Accordingly, the identified predictor importance rankings, nonlinear responses, and interactions should not be assumed to transfer directly to other urban or climatic contexts.

4.5. Limitations and Future Directions

Several limitations should be considered when interpreting the results. First, GloUTCI-M is a machine-learning-derived UTCI product, and some of its input information may overlap with the built-environment predictors used in this study, particularly NDVI, nighttime lights, and land-cover characteristics [37]. Although the additional model m5 (Table S10) analysis indicated relatively stable leading importance rankings among the retained predictors, it does not independently establish the importance of NDVI in the baseline model or fully rule out potential information overlap. Furthermore, the RF, SHAP, and PDP results represent predictive associations rather than causal effects, and the underlying physical

processes were not directly quantified. Future studies using independently derived UTCI estimates, field observations, and process-based simulations could help validate these associations and clarify their physical mechanisms.

Second, the 1 km resolution of GloUTCI-M and its aggregation to urban-centre polygons support national and regional comparisons but cannot resolve neighborhood- or street-scale thermal conditions. Differences in the spatial resolution of UTCI and built-environment datasets may also obscure intra-urban heterogeneity. Although built-up surface area, built-up volume, and building height were included, detailed urban morphology, such as street-canyon geometry and building configuration, was not explicitly represented. Moreover, relative humidity was not included as a separate predictor in the full model. Future research integrating higher-resolution meteorological observations and three-dimensional urban-form data could examine whether the identified associations persist at finer spatial scales.

Third, temporal representativeness remains a limitation. The June–August mean UTCI provides a consistent seasonal indicator but cannot capture short-duration heat extremes, diurnal variations, or conditions outside summer. The four assessment years represent discrete temporal snapshots rather than a continuous record, and differences in UTCI and model-derived associations may reflect both urban environmental changes and interannual meteorological variability. Because the study period ends in 2020, the identified predictor rankings and response patterns may not represent current urban conditions. Future studies incorporating consecutive annual observations, more recent data, and extreme-heat indicators could help assess temporal stability and practical relevance.

Finally, regional modelling and spatial delineation introduce additional limitations. Climate-zone-specific models were developed only for TSH and TH because of the limited sample sizes in TA and TP, restricting regional comparisons to the two major humid climate zones. Fixed 2020 urban-centre boundaries ensured spatial comparability but included areas that were less developed in earlier periods. Future studies with expanded regional samples and year-specific boundaries could further examine thermal associations in arid and high-elevation regions and distinguish urban expansion from changes within established urban areas. In addition, the identified nonlinear response ranges should not be interpreted as universal intervention thresholds or directly transferable planning standards, as they represent model-derived associations that require location-specific validation.

5. Conclusions

Across 1605 GHS-UCDB urban centres in mainland China, mean summer UTCI increased from 29.61 °C in 2005 to 30.43 °C in 2020, with 73.02% of urban centres recording higher values in 2020. The endpoint changes differed across climate zones, with increases of 1.08 °C in TSH and 0.64 °C in TH, compared with slight decreases in TA and TP. These differences highlight the importance of climatic context in understanding the spatial variation of urban thermal stress.

Interpretable Random Forest models revealed substantial spatial and temporal differences in built-environment associations with UTCI. Nationally, NDVI ranked first in predictor importance in 2005 and 2010, whereas surface albedo ranked first in 2015 and 2020. In TSH, NDVI and ImP consistently occupied the leading positions, with NDVI-ImP emerging as the leading interaction during 2010–2020. In TH, the relative importance of albedo, tree cover, urban morphology, and landscape configuration varied across assessment years, accompanied by changes in the leading predictor interactions. These findings indicate that national-level associations do not necessarily represent those within individual climate zones.

Overall, climate-specific modelling provides a useful framework for identifying built-environment characteristics associated with urban thermal stress. However, the identified predictor rankings, nonlinear responses, and interactions represent model-derived associations rather than causal effects or universally applicable intervention thresholds. Further validation using updated environmental data, independent observations, and finer-scale analyses is needed before these findings can inform local urban adaptation strategies.

Supplementary Materials: The following supporting information can be downloaded at https://www.mdpi.com/article/10.3390/rs18223989/s1. Supplementary Material S1: Multicollinearity assessment (Tables S1–S2 and Figure S1); Supplementary Material S2: Multimodel comparison and selection (Table S3 and Figure S2); Supplementary Material S3: Model performance and predictor importance comparisons (Tables S4–S8 and Figure S3); Supplementary Material S4: Sensitivity analysis of potential input-information overlap (Tables S9–S10); Supplementary Material S5: Robustness of leading SHAP interaction pairs (Table S11); Supplementary Material S6: Spatial cross-validation and residual spatial autocorrelation (Table S12).

Author Contributions: Conceptualization, methodology, writing, L.Q. and Z.Z. (Zhigao Zhou); review and editing, Y.C. and Z.Z. (Zhijiang Zhang). All authors have read and agreed to the published version of the manuscript.

Funding: This work was funded by the National Natural Science Foundation of China (No. 42401046), the China Postdoctoral Science Foundation (No. 2025M780303) and the Hubei Provincial Natural Science Foundation (No. 2026AFC1141).

Data Availability Statement: The datasets used in this study are publicly available from their original data providers. Detailed information on the data sources is provided in Section 2.2 and Tables 1 and 2.

Conflicts of Interest: The authors declare no conflicts of interest.

References

1. Chen, Z.; Qiao, R.; Li, S.; Zhou, S.; Zhang, X.; Wu, Z.; Wu, T. Heat and mobility: Machine learning perspectives on bike-sharing resilience in Shanghai. *Transp. Res. Part D Transp. Environ.* **2025**, *142*, 104692. [CrossRef]
2. Yu, X.; Yang, Z.; Xu, D.; Wang, Q.; Peng, J. Urban green spaces enhanced human thermal comfort through dual pathways of cooling and humidifying. *Sustain. Cities Soc.* **2025**, *118*, 106032. [CrossRef]
3. Perkins-Kirkpatrick, S.E.; Lewis, S.C. Increasing trends in regional heatwaves. *Nat. Commun.* **2020**, *11*, 3357. [CrossRef] [PubMed]
4. Sun, H.; Chen, Y.; Li, K.; Gao, S. Spatio-temporal assessment of heat health risk in Chinese metropolitan cities based on the modified multi-indicators coupled risk framework. *Sustain. Cities Soc.* **2024**, *108*, 105451. [CrossRef]
5. Gohain, K.J.; Goswami, A.; Mohammad, P.; Kumar, S. Modelling relationship between land use land cover changes, land surface temperature and urban heat island in Indore city of central India. *Theor. Appl. Climatol.* **2023**, *151*, 1981–2000. [CrossRef]
6. Sun, J.; Xia, J.; Qu, L. Optimizing Urban Green Space Ecosystem Services for Resilient and Sustainable Cities: Research Landscape, Evolutionary Trajectories, and Future Directions. *Forests* **2026**, *17*, 97. [CrossRef]
7. Mora, C.; Dousset, B.; Caldwell, I.R.; Powell, F.E.; Geronimo, R.C.; Bielecki, C.R.; Counsell, C.W.W.; Dietrich, B.S.; Johnston, E.T.; Louis, L.V.; et al. Global risk of deadly heat. *Nat. Clim. Chang.* **2017**, *7*, 501–506. [CrossRef]
8. Peng, J.; Dan, Y.; Yu, X.; Xu, D.; Yang, Z.; Wang, Q. Response of urban green space cooling effect to urbanization in the Three Ring Road area of Changsha City. *Sustain. Cities Soc.* **2024**, *109*, 105534. [CrossRef]
9. United Nations, Department of Economic and Social Affairs, Population Division. *World Urbanization Prospects: The 2018 Revision (ST/ESA/SER.A/420)*; United Nations: New York, NY, USA, 2019. Available online: https://population.un.org/wup/assets/WUP2018-Report.pdf (accessed on 25 May 2026).
10. Chapman, S.C.; Watkins, N.W.; Stainforth, D.A. Warming Trends in Summer Heatwaves. *Geophys. Res. Lett.* **2019**, *46*, 1634–1640. [CrossRef]
11. Hu, Y.; Jia, G.; Gao, H.; Li, Y.; Hou, M.; Li, J.; Miao, C. Spatial characterization of global heat waves using satellite-based land surface temperature. *Int. J. Appl. Earth Obs. Geoinf.* **2023**, *125*, 103604. [CrossRef]
12. Lu, S.; Liu, F.; Ye, Y.; Tang, J.; Li, P.; Lin, W.; Guo, Y.; Ma, R.; Wang, J. Analysis of the Spatio-Temporal Characteristics of Winter Surface Urban Heat Island: A Case Study in Beijing, China. *J. Earth Sci.* **2024**, *35*, 1640–1653. [CrossRef]
13. An, N.; Zuo, Z. Investigating the influence of synoptic circulation patterns on regional dry and moist heat waves in North China. *Clim. Dyn.* **2021**, *57*, 1227–1240. [CrossRef]

14. Luo, M.; Lau, N.C. Increasing Human-Perceived Heat Stress Risks Exacerbated by Urbanization in China: A Comparative Study Based on Multiple Metrics. *Earth's Future* **2021**, *9*, e2020EF001848. [CrossRef]
15. Bröde, P.; Fiala, D.; Błażejczyk, K.; Holmér, I.; Jendritzky, G.; Kampmann, B.; Tinz, B.; Havenith, G. Deriving the operational procedure for the Universal Thermal Climate Index (UTCI). *Int. J. Biometeorol.* **2012**, *56*, 481–494. [CrossRef] [PubMed]
16. Dong, J.; Hu, T.; Liu, Y.; Peng, J. Urban-rural differences in the local human exposure to humid heatwaves in the Northern Hemisphere. *Sustain. Cities Soc.* **2024**, *107*, 105415. [CrossRef]
17. Ullah, S.; You, Q.; Wang, G.; Ullah, W.; Sachindra, D.A.; Yan, Y.; Bhatti, A.S.; Abbas, A.; Jan, M.A. Characteristics of human thermal stress in South Asia during 1981–2019. *Environ. Res. Lett.* **2022**, *17*, 104018. [CrossRef]
18. Hamed, M.M.; Kyaw, A.K.; Nashwan, M.S.; Shahid, S. Spatiotemporal changes in Universal Thermal Climate Index in the Middle East and North Africa. *Atmos. Res.* **2023**, *295*, 107008. [CrossRef]
19. Kyaw, A.K.; Hamed, M.M.; Shahid, S. Spatiotemporal changes in Universal Thermal Climate Index over South Asia. *Atmos. Res.* **2023**, *292*, 106838. [CrossRef]
20. Mohammadi, M.; Khoorani, A. Spatiotemproal changes and hot spots of UTCI index over Iran. *Urban Clim.* **2024**, *56*, 102031. [CrossRef]
21. Shah, A.; Sugathan, A.; Malghan, D.; Kim, R.; Subramanian, S.V. Spatiotemporal changes in heat stress exposure in India, 1981-2023. *Nat. Commun.* **2025**, *16*, 9496. [CrossRef] [PubMed]
22. Wei, D.; Yang, L.; Bao, Z.; Lu, Y.; Yang, H. Variations in outdoor thermal comfort in an urban park in the hot-summer and cold-winter region of China. *Sustain. Cities Soc.* **2022**, *77*, 103535. [CrossRef]
23. Xu, Y.; Tian, L.; Cui, T.; Zhang, J.; Zhang, H.; Wang, Y.; Wang, R. Spatiotemporal characteristics of Universal Thermal Climate Index during five-year return period extreme heat events in the Beijing–Tianjin–Hebei region. *Atmos. Ocean. Sci. Lett.* **2025**, *18*, 100612. [CrossRef]
24. Zhou, S.; Geng, X.; Zhao, J.; Hei, J.; Wu, T.; Chen, Z.; Wu, Z. An LCZ-based machine learning framework for revealing spatial heterogeneity of thermal comfort in high-density areas: Enhancing explainability and fine-grid scale resolution. *Sustain. Cities Soc.* **2025**, *133*, 106873. [CrossRef]
25. Wu, T.; Chen, Z.; Zhou, S.; Huang, R.; Xing, P.; Li, S.; Qiao, R.; Wu, Z. Joint evaluation of urban built environment's driving patterns on urban heat island (UHI) and urban moisture island (UMI). *Sustain. Cities Soc.* **2025**, *127*, 106450. [CrossRef]
26. Zhao, J.; Hu, C.; Li, Z.; Zhang, M.; Fan, H.; Li, K.; Yuan, R. Investigating the quantitative impact of the vegetation indices on the urban thermal comfort based on machine learning: A case study of the Qinhuai River Basin, China. *Sustain. Cities Soc.* **2025**, *125*, 106357. [CrossRef]
27. Ming, Y.; Liu, Y.; Li, Y.; Song, Y. Unraveling nonlinear and spatial non-stationary effects of urban form on surface urban heat islands using explainable spatial machine learning. *Comput. Environ. Urban Syst.* **2024**, *114*, 102200. [CrossRef]
28. Jiang, Y.; Zhang, M.; Peng, L.; Guan, X. Applications and challenges of machine learning in urban thermal environment: A systematic review. *Sustain. Cities Soc.* **2026**, *144*, 107400. [CrossRef]
29. Tanoori, G.; Soltani, A.; Modiri, A. Machine Learning for Urban Heat Island (UHI) Analysis: Predicting Land Surface Temperature (LST) in Urban Environments. *Urban Clim.* **2024**, *55*, 101962. [CrossRef]
30. Lundberg, S.M.; Lee, S.I. A unified approach to interpreting model predictions. In *Proceedings of the 31st International Conference on Neural Information Processing Systems (NIPS'17)*; Curran Associates, Inc.: Red Hook, NY, USA, 2017; pp. 4768–4777.
31. Yin, J.; Wang, H.; Zhang, J. Exploring the thermal effects and influencing factors of urban parks during diurnal variations. *Sustain. Cities Soc.* **2025**, *129*, 106499. [CrossRef]
32. Zhou, Z.; Liang, J.; Yang, Y.; Wang, Z.; Tian, P.; Wang, H. Climate-dependent nonlinear and interactive effects of the urban built environment on urban humid heat stress. *Sustain. Cities Soc.* **2026**, *145*, 107447. [CrossRef]
33. Ding, C.; Wang, M.; Guo, Z.; Chen, N. City size, administrative rank, and Rural–Urban migration in China. *J. Urban Manag.* **2024**, *13*, 3–15. [CrossRef]
34. Ming, Y.; Liu, Y.; Gu, J.; Wang, J.; Liu, X. Nonlinear effects of urban and industrial forms on surface urban heat island: Evidence from 162 Chinese prefecture-level cities. *Sustain. Cities Soc.* **2023**, *89*, 104350. [CrossRef]
35. Melchiorri, M.; Mari Rivero, I.; Florio, P.; Schiavina, M.; Krasnodebska, K.; Politis, P.; Uhl, J.; Pesaresi, M.; Maffenini, L.; Sulis, P.; et al. *Stats in the City: The GHSL Urban Centre Database 2025: Public Release GHS-UCDB R2024*; Publications Office of the European Union: Luxembourg, 2024. Available online: https://data.europa.eu/doi/10.2760/3046391 (accessed on 25 May 2026).
36. Yang, J.; Huang, X. The 30 m annual land cover dataset and its dynamics in China from 1990 to 2019. *Earth Syst. Sci. Data* **2021**, *13*, 3907–3925. [CrossRef]
37. Yang, Z.; Peng, J.; Liu, Y.; Jiang, S.; Cheng, X.; Liu, X.; Dong, J.; Hua, T.; Yu, X. GloUTCI-M: A global monthly 1 km Universal Thermal Climate Index dataset from 2000 to 2022. *Earth Syst. Sci. Data* **2024**, *16*, 2407–2424. [CrossRef]
38. O'brien, R.M. A Caution Regarding Rules of Thumb for Variance Inflation Factors. *Qual. Quant.* **2007**, *41*, 673–690. [CrossRef]
39. Breiman, L. Random forests. *Mach. Learn.* **2001**, *45*, 5–32. [CrossRef]

40. Lundberg, S.M.; Erion, G.; Chen, H.; DeGrave, A.; Prutkin, J.M.; Nair, B.; Katz, R.; Himmelfarb, J.; Bansal, N.; Lee, S.-I. From local explanations to global understanding with explainable AI for trees. *Nat. Mach. Intell.* **2020**, *2*, 56–67. [CrossRef] [PubMed]
41. Cleveland, W.S. Robust locally weighted regression and smoothing scatterplots. *J. Am. Stat. Assoc.* **1979**, *74*, 829–836. [CrossRef]
42. Efron, B.; Tibshirani, R.J. *An Introduction to the Bootstrap*; Chapman & Hall: New York, NY, USA, 1993. [CrossRef]
43. Wang, F.; Gao, M.; Liu, C.; Zhao, R.; McElroy, M.B. Uniformly elevated future heat stress in China driven by spatially heterogeneous water vapor changes. *Nat. Commun.* **2024**, *15*, 4522. [CrossRef] [PubMed]
44. Di Napoli, C.; Pappenberger, F.; Cloke, H.L. Assessing heat-related health risk in Europe via the Universal Thermal Climate Index (UTCI). *Int. J. Biometeorol.* **2018**, *62*, 1155–1165. [CrossRef] [PubMed]
45. Iqbal, J.; Tong, X.; Wang, G.; Ullah, I.; Amin, Y.; Ahmad, I.; Toqeer, M.; Yeboah, E.; Yan, Y.; Cabral, P. Intensifying summer-monsoon human thermal stress across eastern China's major urban agglomerations. *Urban Clim.* **2026**, *70*, 103195. [CrossRef]
46. Liu, H.; Zheng, H.; Wu, L.; Deng, Y.; Chen, J.; Zhang, J. Spatiotemporal Evolution in the Thermal Environment and Impact Analysis of Drivers in the Beijing–Tianjin–Hebei Urban Agglomeration of China from 2000 to 2020. *Remote Sens.* **2024**, *16*, 2601. [CrossRef]
47. Zhai, P.; Yu, R.; Guo, Y.; Li, Q.; Ren, X.; Wang, Y.; Xu, W.; Liu, Y.; Ding, Y. The strong El Niño of 2015/16 and its dominant impacts on global and China's climate. *J. Meteorol. Res.* **2016**, *30*, 283–297. [CrossRef]
48. Zhang, R.; Min, Q.; Su, J. Impact of El Niño on atmospheric circulations over East Asia and rainfall in China: Role of the anomalous western North Pacific anticyclone. *Sci. China Earth Sci.* **2017**, *60*, 1124–1132. [CrossRef]
49. Zhang, P.; Xie, S.-P.; Kosaka, Y.; Lutsko, N.J.; Okumura, Y.M.; Miyamoto, A. Why East Asian monsoon anomalies are more robust in post El Niño than in post La Niña summers. *Nat. Commun.* **2024**, *15*, 7401. [CrossRef] [PubMed]
50. Johansson, E.; Thorsson, S.; Emmanuel, R.; Krüger, E. Instruments and methods in outdoor thermal comfort studies—The need for standardization. *Urban Clim.* **2014**, *10*, 346–366. [CrossRef]
51. Luo, M.; Wu, S.; Liu, Z.; Lau, N.C. Contrasting Circulation Patterns of Dry and Humid Heatwaves Over Southern China. *Geophys. Res. Lett.* **2022**, *49*, e2022GL099243. [CrossRef]
52. Zhao, J.; Zhao, X.; Wu, D.; Meili, N.; Fatichi, S. Satellite-based evidence highlights a considerable increase of urban tree cooling benefits from 2000 to 2015. *Glob. Change Biol.* **2023**, *29*, 3085–3097. [CrossRef] [PubMed]
53. Leng, S.; He, H.; Huete, A.; Pinagé, E.R.; Zhang, W.; Ding, H.; Chen, L.; Sun, R. Diminishing cooling returns of urban greening amid a warming climate. *Proc. Natl. Acad. Sci. USA* **2026**, *123*, e2616535123. [CrossRef] [PubMed]
54. Yang, Q.; Huang, X.; Yang, J.; Liu, Y. The relationship between land surface temperature and artificial impervious surface fraction in 682 global cities: Spatiotemporal variations and drivers. *Environ. Res. Lett.* **2021**, *16*, 024032. [CrossRef]
55. Wu, Y.; Zong, Q.; Wang, J.; Wang, S.; Jin, K.; Liu, Q. Spatial patterns and drivers of surface urban heat islands in East China: A county-level study based on the RH-SHAP model. *Int. J. Climatol.* **2026**, *46*, e70594. [CrossRef]
56. Li, Y.; Svenning, J.C.; Zhou, W.; Zhu, K.; Abrams, J.F.; Lenton, T.M.; Ripple, W.J.; Yu, Z.; Teng, S.N.; Dunn, R.R.; et al. Green spaces provide substantial but unequal urban cooling globally. *Nat. Commun.* **2024**, *15*, 7108. [CrossRef] [PubMed]
57. Mohamed, A.; Lorestani, N.; Shabani, F. Impact of urbanization on land surface temperature: A global perspective. *Curr. Res. Environ. Sustain.* **2025**, *10*, 100315. [CrossRef]
58. Zhang, Y.; Silva, C.A.; Chen, M. Analyzing Thermal Environment Contributions and Driving Factors of LST Heterogeneity in Different Urban Development Zones. *Remote Sens.* **2024**, *16*, 2973. [CrossRef]
59. Wang, W.; Li, X.; Li, C.; Gan, D. Opposing Impacts of Greenspace Fragmentation on Land Surface Temperature in Urban and Surrounding Rural Areas: A Case Study in Changsha, China. *Remote Sens.* **2024**, *16*, 3609. [CrossRef]
60. Schrijvers, P.J.C.; Jonker, H.J.J.; de Roode, S.R.; Kenjereš, S. The effect of using a high-albedo material on the Universal Temperature Climate Index within a street canyon. *Urban Clim.* **2016**, *17*, 284–303. [CrossRef]
61. Yao, L.; Sailor, D.J.; Yang, X.; Xu, G.; Zhao, L. Are water bodies effective for urban heat mitigation? Evidence from field studies of urban lakes in two humid subtropical cities. *Build. Environ.* **2023**, *245*, 110860. [CrossRef]
62. Roberts, D.R.; Bahn, V.; Ciuti, S.; Boyce, M.S.; Elith, J.; Guillera-Arroita, G.; Hauenstein, S.; Lahoz-Monfort, J.J.; Schröder, B.; Thuiller, W.; et al. Cross-validation strategies for data with temporal, spatial, hierarchical, or phylogenetic structure. *Ecography* **2017**, *40*, 913–929. [CrossRef]

Disclaimer/Publisher's Note: The statements, opinions and data contained in all publications are solely those of the individual author(s) and contributor(s) and not of MDPI and/or the editor(s). MDPI and/or the editor(s) disclaim responsibility for any injury to people or property resulting from any ideas, methods, instructions or products referred to in the content.